10-1-2021

Design of gate-tunable graphene electro-optical reflectors based on an optical slot-antenna coupled cavity

Tao Fang
Thayer School of Engineering at Dartmouth

Xiaoxue Gao
Thayer School of Engineering at Dartmouth

Xiaoxin Wang
Thayer School of Engineering at Dartmouth

Jifeng Liu
Thayer School of Engineering at Dartmouth

Design of gate-tunable graphene electro-optical reflectors based on an optical slot-antenna coupled cavity

Journal of Physics: Photonics

OPEN ACCESS

RECEIVED
16 April 2021

REVISED
30 August 2021

ACCEPTED FOR PUBLICATION
14 September 2021

PUBLISHED
14 October 2021

PAPER

Design of gate-tunable graphene electro-optical reflectors based on an optical slot-antenna coupled cavity

Tao Fang, Xiaoxue Gao, Xiaoxin Wang and Jifeng Liu*

Thayer School of Engineering, Dartmouth College, Hanover, NH 03755, United States of America
* Author to whom any correspondence should be addressed.

E-mail: jifeng.liu@dartmouth.edu

Keywords: graphene, nanodots, optical reflective resonator, optical slot-antenna-coupled cavity (SAC), Tunable photonic surfaces

Supplementary material for this article is available online

Abstract

The unique properties of graphene offer an exciting opportunity towards tunable photonic surfaces for flexible devices. In this paper, we design a gate-tunable, free-space graphene electro-optical reflector based on cavity resonator structures. We firstly calculate the graphene refractive index n and k as a function of Fermi level and external gating voltage. Then, we designed the structure of the single-layer graphene reflective resonator by carefully selecting suitable materials and device parameters to maximize the reflectance differences before and after electro-optical tuning. We also developed a theoretical model to discuss this system based on the optical transition matrix method. Moreover, we used field enhancement to further increase the reflectance differences by incorporating Sn nanodots based optical slot-antenna coupled cavities. The maximum broadband, incident angle insensitive reflectance differences could reach 28% with an extinction ratio of 1.62 dB at a low insertion loss of 0.45 dB, and the spectral range is tunable by changing the optical cavity length. We also used an indium tin oxide layer as part of the optical cavity and the electrode simultaneously to reduce the voltage applied. To our best knowledge, this work is the first one on tunable two-dimensional (2D) material reflectors for free-space applications, apart from using liquid crystals or magnetic metasurfaces. This new design of tunable 2D electro-optical reflectors also reduces the complexity of fabrication steps, having promising applications in tunable flexible photonic surfaces and devices for variable optical attenuators and light detection and ranging systems.

1. Introduction

Graphene is a two-dimensional (2D) material consisting of one layer of carbon atoms in a hexagonal lattice [1, 2]. Unlike other similar 2D materials, single-layer graphene (SLG) has a special band structure. The band gap for the SLG is zero and there is a Dirac cone near the Fermi level [3–5], while for other 2D materials like transition metal dichalcogenides (TMDC) and black phosphorus (BP), the band structure remains similar to regular semiconductors with non-zero bandgaps [6–8]. As a result, the Fermi level and carrier density for SLG are easily tunable by external gate voltage [9, 10]. Until now, several theoretical and experimental works have been done on the gate tunable graphene properties. For example, Geim *et al* calculated the optical conductivity of graphene as a function of Fermi level based on the tight-binding model [11]. Wang *et al* explored the gate-variable optical transitions in graphene experimentally [12]. Liu *et al* fabricated a graphene broadband optical modulator based on the gate tunable absorption [13]. An interesting potential application of such properties is gate-tunable SLG reflectors. In previous literature, tunable reflectors have been investigated using liquid crystal or magnetic metasurfaces [14, 15], while free-space tunable 2D reflectors offer unique advantages of ultrathin thickness and mechanical flexibility. These 2D devices also have promising applications in variable optical attenuators (VOAs) or tunable reflectors for light detection and

ranging (LiDAR) systems. The key limitation, though, is the relatively low electro-absorption effect of SLG under vertical incidence, where the absorption can be changed by ~2% at most.

Optical cavity is a very important part in optical devices to enhance light–matter interaction [16]. Traditional Fabry–Perot optical cavity consists of two high-reflective metal layers and one dielectric layer in the middle. To tune the optical cavity behavior, we can change the reflective index of the dielectric, and the reflectance will change [17, 18]. Another idea is changing the reflectance of the metal layer directly. Intrinsic graphene behaves like a semimetal optically [19, 20], and it can be converted to a dielectric if we apply enough gate voltage on it. Although graphene is very thin, we can still construct a graphene/dielectric interface whose optical property would change a lot before and after tuning. If we couple this interface with an optical cavity, we have a gate-tunable reflective resonator. This tunable resonator is different from traditional resonator because it is based on the high refractive index change for graphene, i.e. the metallic layer instead of the dielectric layer, before and after gate voltage applied.

In this paper, we design and optimize the graphene reflective resonator towards gate-tunable reflectors based on 2D materials. We start this discussion from the graphene reflective index as a function of its Fermi level, and the relation between graphene Fermi level and external gate voltage. Then, we examine each part of the resonator carefully. We use vector analysis to find the tuning limit in this system, and we also select suitable materials for the resonator. Finally, we optimize the structure based on Sn-nanodots optical slot-antenna coupled cavities (SAC) previously demonstrated by our group to benefit from the strong field enhancement in graphene [21]. An interesting feature of the optical SAC structure is that the tunable reflectance spectrum is almost independent of the incidence angle compared to conventional optical cavities. Moreover, we discuss some strategies to reduce the gate voltage applied, including incorporating indium tin oxide (ITO) conductive layer as part of the optical cavity and the electrode simultaneously.

2. Method

OpenFilter and COMSOL Wave Optics Module are used in this simulation. OpenFilter involves the optical transition matrix model to calculate the reflection, transmission and absorption in two-dimensional infinite plane. The reflective index and thickness for each layer are the input parameters. COMSOL utilizes the finite-element method to solve the Maxwell equation in three-dimensional space. We define the geometric parameters, refractive index in each region and suitable boundary conditions (periodic condition in the graphene plane and scattering boundary condition normal to the graphene plane) in the simulation. The reflection and transmission are calculated by comparing the power input and output.

3. Graphene refractive index model

As mentioned earlier, SLG behaves like a Dirac semimetal. The energy band diagram is linear near the Fermi level, and the slope is the Fermi velocity times the reduced Plank constant $\hbar$. The Fermi velocity is $v_F = 9 \times 10^5 \mathrm{m\ s^{-1}}$ for graphene [11, 22, 23]. This band structure is called Dirac cone (figure 1(a)). The 2D normalized density of state can be calculated by definition,

$$\frac{N(E)}{S} = \frac{2g_v}{4\pi^2} \int \delta\left(E - E_k\right) 2\pi k \mathrm{d}k. \tag{1}$$

Here S is the SLG area, $g_v = 2$ is the number of degeneracy for the band structure of SLG, and we have an additional factor of 2 because of spin. Considering $k = \frac{2\pi E_k}{h v_F}$ and $\mathrm{d}k = \frac{2\pi \mathrm{d}E_k}{h v_F}$, we can solve this integral as,

$$\frac{N(E)}{S} = \frac{2}{\pi h^2 {v_F}^2} |E| = 2.25 |E| \ \mathrm{eV^{-1}nm^{-2}} \tag{2}$$

where energy E is in the unit of eV here.

In this paper, we use an inherently p-type SLG from chemical vapor deposition, where the Fermi level is 0.251 eV below the Dirac point from our previous experimental data [21, 24, 25]. This kind of SLG is also used in the previous experimental work of other researchers [12, 13] and it can reduce the voltage applied for SLG transparency in the near infrared (NIR) regime. We would like to apply a positive gate voltage such that the Fermi level will drop to some extent. The hole density change is calculated by the integral of Fermi–Dirac distribution multiplying density of state,

$$\Delta p = \int \frac{N(E)}{S} f(E)\, \mathrm{dE}, \tag{3}$$

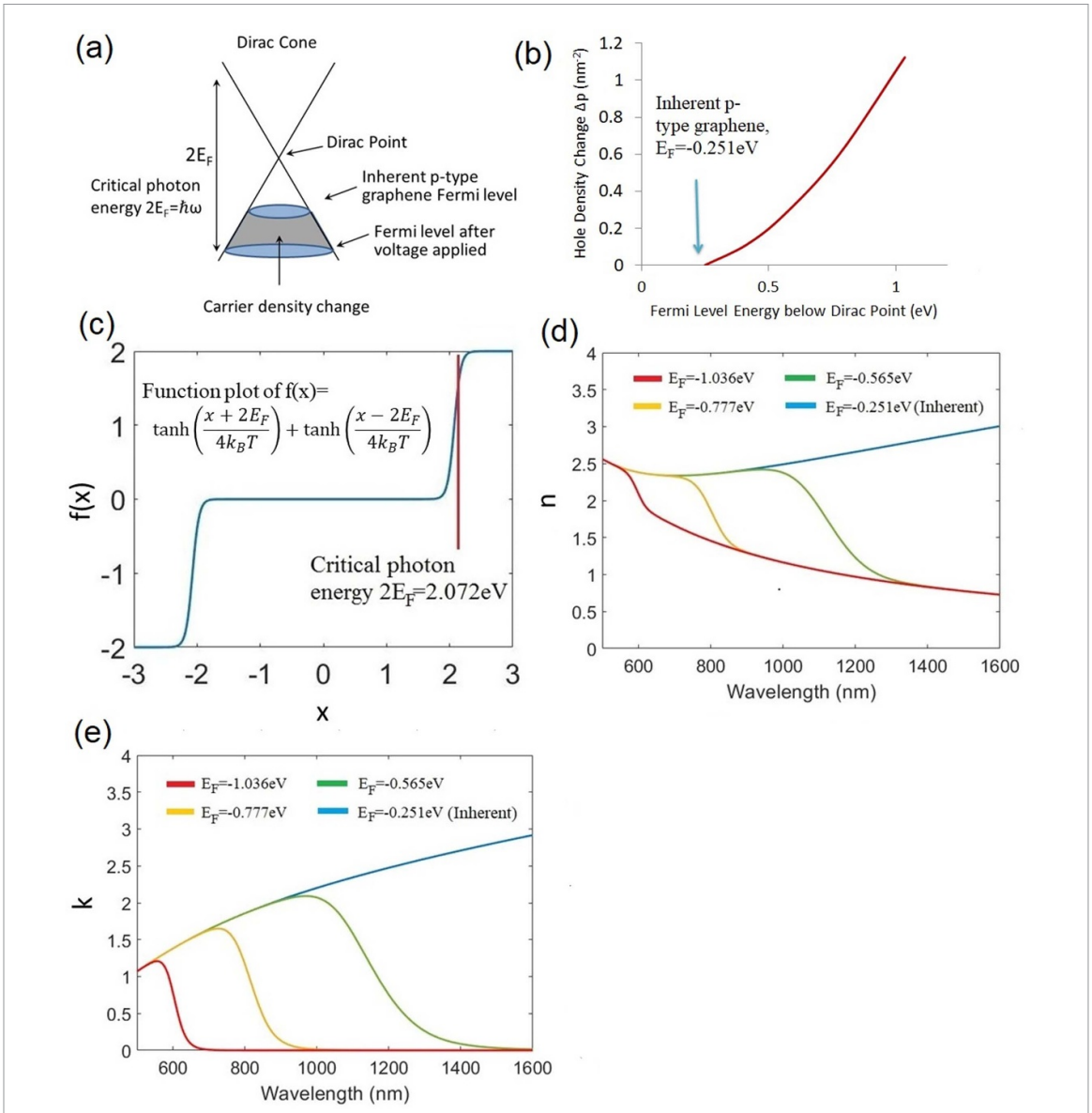

Figure 1. (a) Illustration of the graphene band structure and the carrier density change. (b) Plot of the carrier density change as a function of the Fermi level. (c) Plot of the relative magnitude of the optical conductivity for the function $f(x)$. The critical photon energy $\hbar\omega = 2E_F$ is shown on the graph. This critical value greatly influences the absorption spectrum. (d) Real part of the graphene reflective index. The Fermi levels are set to be −0.251 eV (inherent), −0.565 eV (critical wavelength 1100 nm), −0.777 eV (critical wavelength 800 nm) and −1.036 eV (critical wavelength 600 nm). (e) Corresponding imaginary part of the graphene reflective index.

where $f(E)$ is the Fermi–Dirac distribution function. Notice that the inherent Fermi level is not zero. For convenience, we do an energy shift for the integral,

$$N(E) = -2.25\,(E - 0.251)\ \mathrm{eV}^{-1}\mathrm{nm}^{-2}. \tag{4}$$

If we assume that the Fermi level is t eV below Dirac point after tuning, the hole density changed is

$$\Delta p = \int_{-t+0.251}^{0} \frac{-2.25\,(x - 0.251)}{\mathrm{e}^{\frac{x}{0.026}} + 1}\mathrm{d}x \tag{5}$$

at room-temperature (i.e. $k_B T = 0.026$ eV).

We did the integral numerically for different t values. The function plot of Δp versus t is shown in figure 1(b).

The reflective index is modeled by a semi-analytical formula. As we know, the reflective index is the square root of the relative dielectric function. For the imaginary part, Geim *et al* has calculated the optical conductivity by the tight-binding model [11]

$$\sigma = \frac{\pi e^2}{4h}\left(\tanh\left(\frac{h\omega + 2E_F}{4k_B T}\right) + \tanh\left(\frac{h\omega - 2E_F}{4k_B T}\right)\right). \tag{6}$$

The imaginary part of the dielectric function is the optical conductivity divided by the thickness of graphene, which is 0.335 nm [26, 27]. If we set $E_F = -1.036$ eV, we can plot the function $f(x) = \tanh\left(\frac{x+2E_F}{4k_B T}\right) + \tanh\left(\frac{x-2E_F}{4k_B T}\right)$ to have an intuition of the optical conductivity relative magnitude (figure 1(c)).

From the plot we can see that there is a critical photon energy $2E_F$ corresponding to the interband transition from $-E_F$ to $+E_F$, as shown on the graph. Below this value, the optical conductivity is almost zero while above this value, the optical conductivity is not zero. Since the real part of the dielectric function is less determined by the Fermi level, this critical photon energy greatly influences the graphene absorption spectrum and the imaginary part of the reflective index.

For the real part of the dielectric function, it relates to the bounded electron, so we assume that it is not a function of the Fermi level. We fit the real part by the polynomial function from previous experimental work [28–30]. Combining the real part and the imaginary part, we take a square root of the relative dielectric function and get the reflective index. The plot of reflective index $n + ik$ versus the wavelength is shown in figures 1(d) and (e) with different Fermi levels. Besides the p-type graphene before gating, the other three Fermi levels are set to be -0.565 eV (critical photon wavelength 1100 nm), -0.777 eV (critical photon wavelength 800 nm) and -1.036 eV (critical photon wavelength 600 nm) upon gating.

From the graph, the k values will drop to zero and the graphene behaves like a dielectric if the wavelength is larger than the critical wavelength. With lower Fermi level, the drop is steeper. We can control the graphene n and k by applying suitable gate voltage, which is the starting point of this paper. In the next discussion, the 'reflective index before tuning' corresponds to the inherent graphene reflective index (blue curve), and the 'reflective index after tuning' corresponds to the 600 nm critical wavelength reflective index (red curve). Clearly, with refractive index tuning, graphene behaves like a dielectric in the NIR region in that n is finite and k is ~0. Therefore, electrical tuning changes SLG from a semimetal to a dielectric in the NIR spectral regime.

At the end of this section, we briefly calculate the magnitude of the gate voltage by the parallel capacitor model,

$$\mathrm{U} = \frac{Q}{C} = \frac{\Delta p \mathrm{Se}}{\frac{\varepsilon_0 \varepsilon_r S}{d}} = \frac{\Delta p \mathrm{ed}}{\varepsilon_0 \varepsilon_r}. \tag{7}$$

It is proportional to the hole density change Δp in (5), distance d between the two plates and inversely proportional to the dielectric constant ε_r. If we use the same device structure as that in [12] ($d = 7$ nm, $\varepsilon_r = 8.5$ for Al_2O_3) and set the critical wavelength to be 600 nm, the voltage applied is 16.72 V. It is a reachable value and not extremely large. We will discuss more and give the strategies to reduce the gate voltage in the parameter optimization part.

4. Theoretical model for reflectance difference upon tuning and material selection

From the discussion in the last section, graphene has a very large reflective index change (Δn and Δk) before and after tuning. It is very natural to build an interface of graphene with two dielectrics on both sides (figure 2(a), left bottom), one of the dielectric being the medium of incident light while the other being part of the optical cavity. The reflective indexes n_1 and n_2 are no less than 1, and one of them might be air. If we assume the reflective coefficients (vectors in the complex plane) are $\boldsymbol{a}$ and $\boldsymbol{b}$ before and after tuning, the reflectance difference δ is

$$\delta = \left|\boldsymbol{a}^2 - \boldsymbol{b}^2\right|. \tag{8}$$

It is difficult to get a large δ in the simulation by simply changing n_1 and n_2. The reason is we do not make use of the phase difference. For example, if $\boldsymbol{a} = E_0\exp(i\pi/2)$, $\boldsymbol{b} = E_0\exp(i\pi)$, δ is just zero but the phase difference is $\pi/2$. To take advantage of the phase difference, we can add a backside reflection in this system. The cavity length L might be changed to control the phase of the backside reflection (figure 2(a)). To simplify the analysis, we assume the backside reflection coefficient $\boldsymbol{c}$ is unchanged before and after tuning. Therefore, the reflectance difference δ is

$$\begin{aligned}\delta &= (\boldsymbol{a}+\boldsymbol{c})^2 - (\boldsymbol{b}+\boldsymbol{c})^2 \\ &= (\boldsymbol{a}-\boldsymbol{b})(\boldsymbol{a}+\boldsymbol{b}+2\boldsymbol{c}) \\ &= (\boldsymbol{a}-\boldsymbol{b})(\boldsymbol{a}+\boldsymbol{b}) + 2(\boldsymbol{a}-\boldsymbol{b})\boldsymbol{c}.\end{aligned} \tag{9}$$

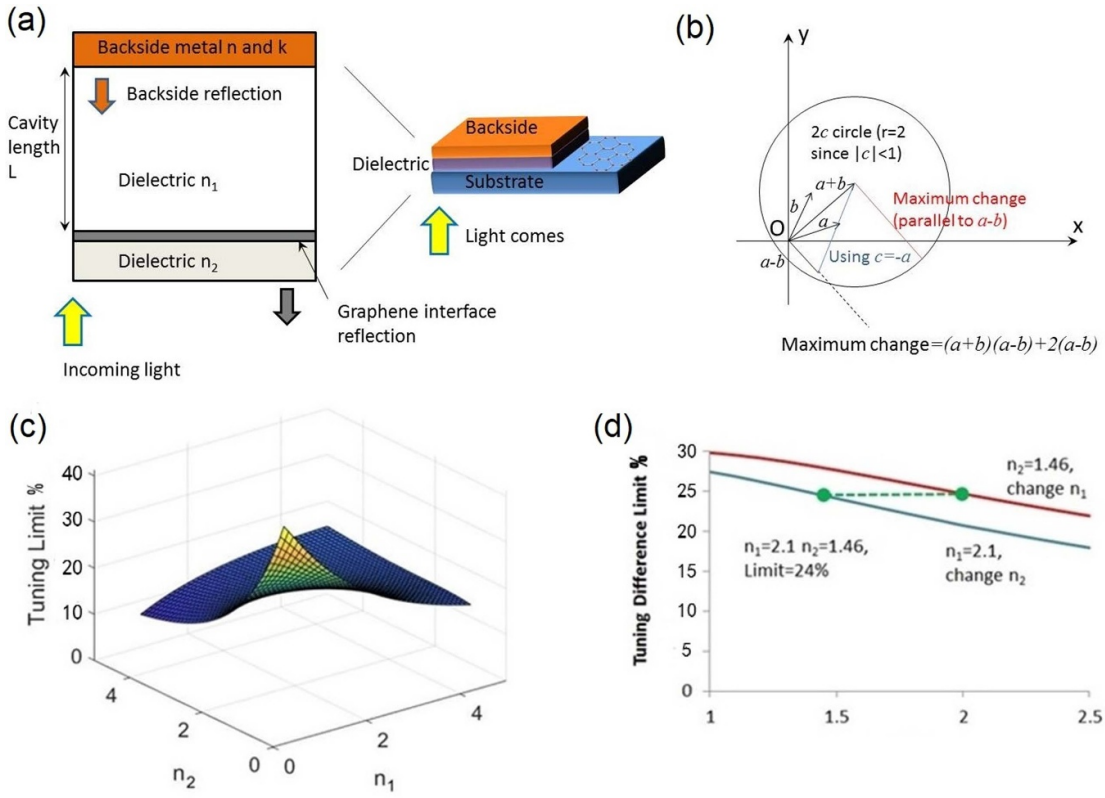

Figure 2. (a) Structure illustration of the optical cavity. It consists of graphene, two dielectrics and backside metal. (b) Vector analysis of the reflectance difference. To get the maximum δ, the vector c should be parallel to the vector (a) and (b). (c) The tuning limit $\delta_{max} = |\boldsymbol{a}^2 - \boldsymbol{b}^2| + 2|\boldsymbol{a} - \boldsymbol{b}|$ as a function of n_1 and n_2. The left axis is n_2 while the right axis is n_1. The analysis is performed at 1550 nm wavelength. (d) Cutting line $n_1 = 2.1$ and $n_2 = 1.46$ of figure (c). The intersecting lines between the surface in figure 2(c) and the planes of $n_1 = 2.1$ (blue) and $n_2 = 1.46$ (red). The green dashed line shows the case for $n_1 = 2.1$ and $n_2 = 1.46$.

We briefly analyze this expression by drawing these vectors on the complex plane (figure 2(b)). The vector ***a, b, a*** + ***b*** and ***a***−***b*** are denoted on the graph. If the dielectric is fixed, n_1 and n_2 are fixed, so the vector ***a, b, a*** + ***b*** and ***a***−***b*** are fixed. Since $|\boldsymbol{c}| < 1$ and the phase is arbitrary, the vector $\boldsymbol{a} + \boldsymbol{b} + 2\boldsymbol{c}$ lies in a circle. We can select $\boldsymbol{c} = -\boldsymbol{a}$ or $\boldsymbol{c} = -\boldsymbol{b}$, which means matching the reflectance at both sides and the reflectance is zero, just as the blue line on the graph. However, this is not the maximum reflectance difference. To maximize the reflectance difference δ, the vector c should be parallel to the vector $a-b$, and the maximum difference is no larger than

$$\delta_{max} = |\boldsymbol{a}^2 - \boldsymbol{b}^2| + 2|\boldsymbol{c}|_{max}|\boldsymbol{a} - \boldsymbol{b}| < |\boldsymbol{a}^2 - \boldsymbol{b}^2| + 2|\boldsymbol{a} - \boldsymbol{b}|. \quad (10)$$

Comparing (10) with (8), we have an additional term $2|\boldsymbol{a}-\boldsymbol{b}|$ in the expression. Since $|\boldsymbol{a}|$ and $|\boldsymbol{b}|$ are not very large (0.05–0.3), this additional term greatly increases the reflectance difference by making use of the phase difference. This analysis clearly shows the advantage of adding the backside reflector to form an optical cavity.

Moreover, δ_{max} is larger if $|\boldsymbol{c}|$ is larger. It is better to use a good metal in the backside. A good metal has low n values and high k values such that there is a large reflection at the dielectric-metal interface. Another point is that the normal incidence is needed to maximize the $|\boldsymbol{c}|$ value. In the following discussion, we use the normal incidence if not specified. We can plot the tuning limit $\delta_{max} = |\boldsymbol{a}^2 - \boldsymbol{b}^2| + 2|\boldsymbol{a} - \boldsymbol{b}|$ as a function of n_1 and n_2 in a certain wavelength. The vector ***a*** and ***b*** are calculated by analytical model. Figure 2(c) shows the three-dimensional plot for the wavelength of 1550 nm.

From the plot, the tuning limit δ_{max} is around 20%−25%. If n_1 and n_2 are both between 1.3 and 2.5 (common dielectrics), the tuning limit δ_{max} will not change a lot in this range. In addition, n_1 should not be very small; otherwise the cavity length has to increase for the same phase shift and the voltage applied will be larger (see formula 7). So there is a trade-off here for n_1. To fabricate easily, we select the substrate to be silica and the material inside the cavity to be tin dioxide so n_1 around 2.1 and $n_2 = 1.46$. The exact refractive index of tin dioxide is fitted from experimental data in our group (see supplementary materials for more details).

Table 1. Reflectance value of tin dioxide and different metal interfaces in the wavelength 1550 nm.

Metal	n	k	R
Ag	0.14	11.37	0.971
Au	0.52	10.74	0.942
Al	1.58	15.65	0.936
Pb	1.70	8.59	0.813
Zn	4.89	11.99	0.778
Sn	3.24	9.02	0.739
Ni	3.09	7.72	0.695
Fe	3.11	5.24	0.510
Mn	3.74	5.30	0.480
Ti	3.68	4.61	0.424
Bi	6.24	4.52	0.414

We can also plot the intersecting lines between the surface in figure 2(c) and the planes of $n_1 = 2.1$ and $n_2 = 1.46$. (shown in figure 2(d)).

For the backside, table 1 summarizes the reflectance value of tin dioxide and common metal interfaces at the wavelength of 1550 nm. The metal n and k values are adapted from the reflective index database [31–37].

From table 1, silver has the largest R value among all the metals. Therefore, we use silver as the backside metal.

Finally, we would like to point out that this tuning difference model is a preliminary model. Some factors are not considered in this model. For example, because of transmission difference before and after tuning, the backside reflection coefficient $\boldsymbol{c}$ is not exactly the same. However, this model gives the basic idea of material selection, and the tuning limit (∼24%) is confirmed in the following simulation by the optical transition matrix model. Moreover, this model clearly shows why we need a backside reflection by comparing formulas (8) and (10). As a result, this model is still an effective way to analyze this system.

5. Structure and parameters optimization

5.1. Thickness effect

After selecting the materials, now we come to optimize the structure. Apart from the silica substrate, we need to determine the thicknesses of tin dioxide and backside silver. For the backside silver, it should be sufficiently thick to avoid transmission at this side. Figure 3 shows a 100 nm SnO_2 test optical cavity structure with different silver thickness values,

From figure 3, if the Ag thickness is larger than 60 nm, we can say there is no transmission at this side and the thickness effect is very small. In the next simulation, we use 100 nm silver at the back side.

The SnO_2 thickness will influence the backside reflection phase and the interference order. To study it systematically, we estimate the maximum thickness of SnO_2 in the following way: The wavelength range is between 500 nm and 1600 nm and the n value for SnO_2 is between 2 and 2.5. For one cycle (phase changes by 2π), $2nt = \lambda_{max} = 1600$ nm, so t is no larger than 1600/2/2 = 400 nm. We simulate the thickness L from 50 nm to 400 nm with 50 nm interval (figure 4).

According to figure 4, the reflectance before tuning is smaller than that after tuning. The reason is that SLG has more absorption before tuning, which reduces the reflectance. From figure 4(c), the incidence angle does not influence the spectrum significantly. From figure 4(d), the broadband reflectance difference is around 18%. The thickness dependence is just similar to the regular optical cavity. The red curves ($L = 50$ nm, 100 nm and 150 nm) are the first order, and there is only one large peak between the wavelength range 500 nm to 1600 nm for these curves. Similarly, the yellow curves ($L = 200$ nm, 250 nm and 300 nm) are the second order and the blue curves ($L = 350$ nm and 400 nm) are the third order. The reflectance differences for the first order are larger than those in higher orders in the same wavelength. Therefore, we keep the SnO_2 thickness 50 nm, 100 nm and 150 nm structures in the next optimization procedures. In the real application, we can change the thickness of SnO_2 to match the target wavelength we intend, as figure 4(d) shows.

5.2. Increase the reflectance difference by field enhancement in optical SAC structures

In our group's previous work, we used Sn nanodot-based optical structures to dramatically increase the graphene absorption under vertical incidence [21, 24, 25]. The nanogaps between ultrahigh refractive index Sn nanodots acts as optical slot antenna that couples with the optical cavity to strongly enhance the electromagnetic field in the SLG region. Generally speaking, smaller gaps between nanodots are beneficial for

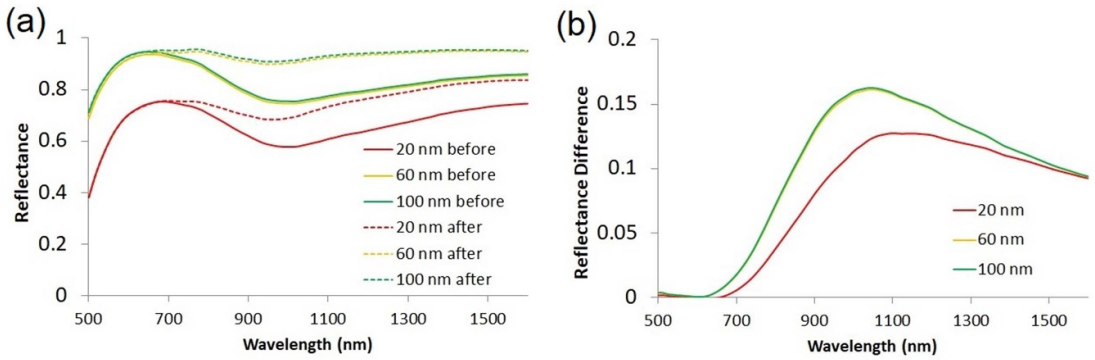

Figure 3. 100 nm SnO_2 test optical cavity structure (silica-SLG-SnO_2–Ag) with 20 nm, 60 nm and 100 nm at back side. (a) Reflectance before and after tuning. (b) Reflectance difference.

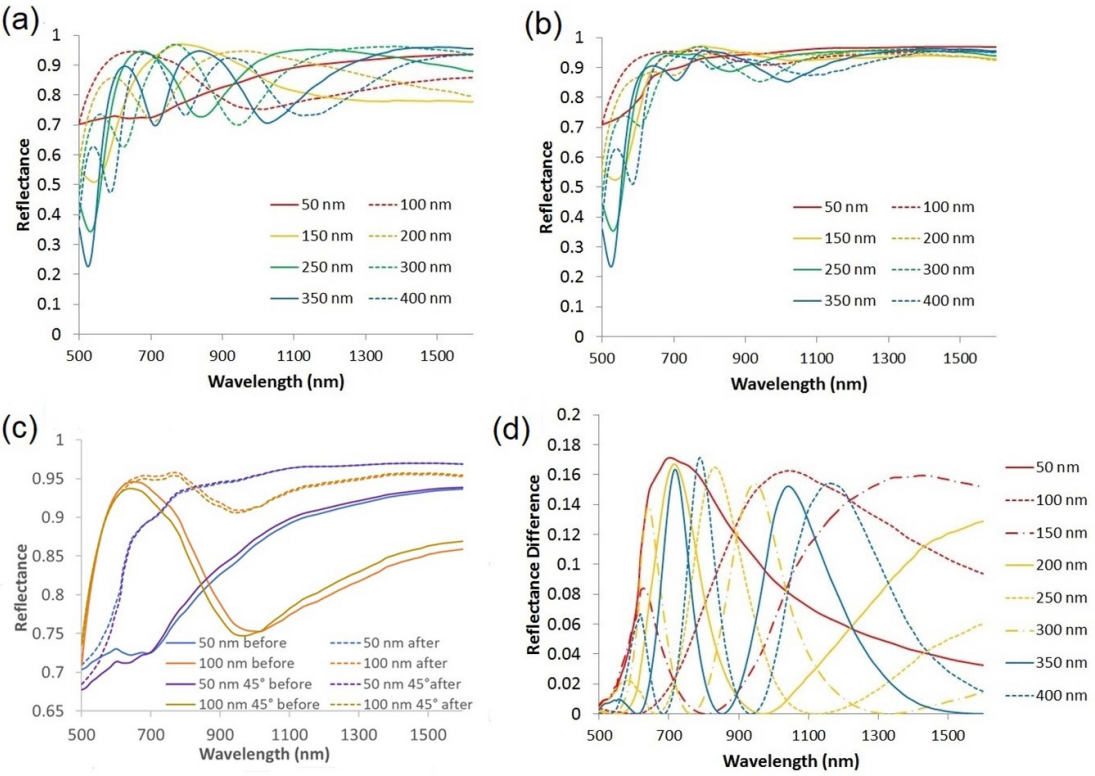

Figure 4. SnO_2 thickness effect. The Fermi level before tuning is 0.251 eV below the Dirac point and after tuning is 1.036 eV below the Dirac point separately. (a) Reflectance before tuning with eight different thicknesses. (b) Reflectance after tuning with eight different thicknesses. (c) Comparison of reflectance changes for 50 nm and 100 nm SnO_2 structures under normal incident and 45° incidence angle. (d) Reflectance difference with eight different thicknesses.

local field enhancement. On the other hand, very tiny gaps $\ll$10 nm would be difficult to achieve experimentally. Therefore, in this design we use a Sn nanodots size and spacing experimentally achieved in our previous work [21, 25], as shown in figure 5(c). We use 9 nm nanogaps between the Sn nanodots in the simulation. The radius and height of the Sn nanodots are 40.5 and 30 nm, respectively. We note that these parameters could be further optimized if better control of self-assembly can be implemented. The absorption for intrinsic graphene (graphene suspended in air) is $\pi\alpha = 2.3\%$, where α is the fine structure constant, around 1/137 [38, 39]. For the graphene on silica substrate, the absorption could be increased from $\sim$2% to nearly 20% in the infrared region by utilizing this tin nanodots optical SAC structure (figure 5(a)) [25].

We can use a similar strategy to increase the reflectance difference. Since this model is the field enhancement model, the reflectance difference may exceed the tuning limit calculated in the last section because the tuning difference model is calculated by the optical transition matrix model without considering near field enhancement. The idea is to maximize the electromagnetic field in SLG in order to sample a larger change in reflectance when it is tuned transparent. Since we have a smaller absorption from SLG after tuning,

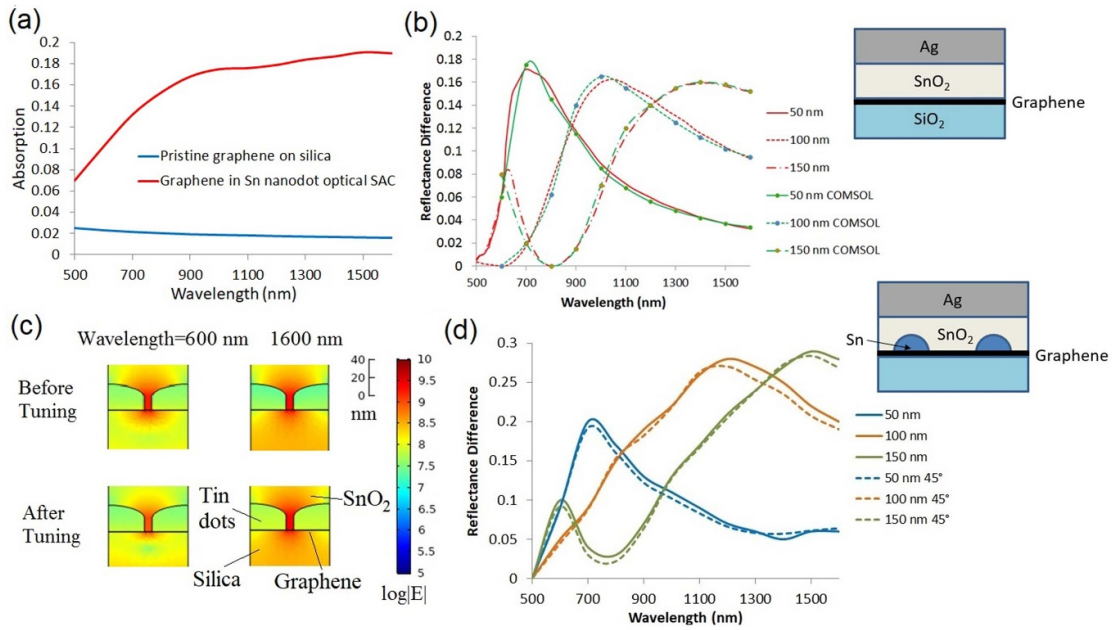

Figure 5. (a) Enhanced graphene absorption on silica substrate by incorporating Sn nanodots optical SAC structure (red line) compared to that of pristine graphene on silica (blue line) [25]. The cross-section of the Sn nanodots is shown in (c). We use 9 nm nanogaps between the Sn nanodots in the simulation. The radius and height of the Sn nanodots are 40.5 and 30 nm, respectively. These parameters are based on the experimentally demonstrated Sn nanodot structures in [21] and [25]. (b) Reflectance differences of 50 nm, 100 nm, and 150 nm SnO_2 optical cavity without tin dots, confirmed by COMSOL optical transition matrix model. (c) Electric field plot of two wavelengths (600 nm, 1600 nm) before and after tuning. The scale bar is uniform and identical in vertical and horizontal directions. (d) Enhanced reflectance difference plot for Sn nanodot optical SAC structures including the 45 degrees incidence results. This is the maximum reflectance difference we reached in this paper.

the reflectance increases correspondingly. The larger the field enhancement in SLG, the greater the reflectance change. From the *E*-field magnitude plot (figure 5(c)), the wavelength of 1600 nm (infrared) has a larger field enhancement than that that of 600 nm (visible light), which coincides with our previous experimental data [21, 24, 25]. The larger absorption in the NIR region corresponds to a larger optical response, so the reflectance difference is also larger in this region when graphene is made transparent upon gating. Figure 5(d) shows the reflectance differences with Sn nanodot optical SAC. Comparing figure 5(d) with figure 5(b), the peak reflectance difference increases by ∼10%, and the peak position is red-shifted because of the lateral scattering effect of the Sn nanodots that is equivalent to elongating the cavity length [21]. In figure 5(d), the 45° incidence results also do not differ much from the normal incidence result. The peak value is slightly smaller and the peak position is slightly blue-shifted. This tendency is similar to that in figure 4(c). More data on the reflectance spectra at different incidence angles are shown in figure S2 (available online at stacks.iop.org/JPPHOTON/3/045003/mmedia) in the supporting information, indicating little change in reflectance spectra as the incidence angle increases from 0 to 75°. Therefore, the tunable optical SAC reflector performance is insensitive to the incidence angle, which offers convenience in practical applications. This phenomenon is due to the scattering and strong field enhancement offered by the Sn nanodots, which reduces the sensitivity to the original incident angles. In the following, we use the normal incidence to further optimize the structure.

5.3. Optimization of gating voltage

In this system, another important topic is the gating voltage applied. In the first section, we have calculated the carrier density, which is proportional to the voltage applied. Furthermore, the voltage depends on the distance between two parallel plates and the relative dielectric constant ε_r. From the design above, we can apply a voltage on the graphene and the backside metal. However, this will give an extremely large voltage, since the dielectric is very thick.

We plan to optimize this structure by incorporating an ITO layer as both part of the optical cavity and the conductive electrode simultaneously. ITO is a conductive material and has a low imaginary part of the refractive index [40]. Here we used the ITO glass CG-60IN-CUV in the simulation, whose refractive index is measured by a general oscillator layer with VASE software in [40]. Therefore, with the ITO layer, the optical path length can keep the same but the distance between two electrodes will greatly decrease, so the voltage will decrease. Figure 6(a) shows a schematic structure. In this case, both SnO_2 and ITO contribute to the

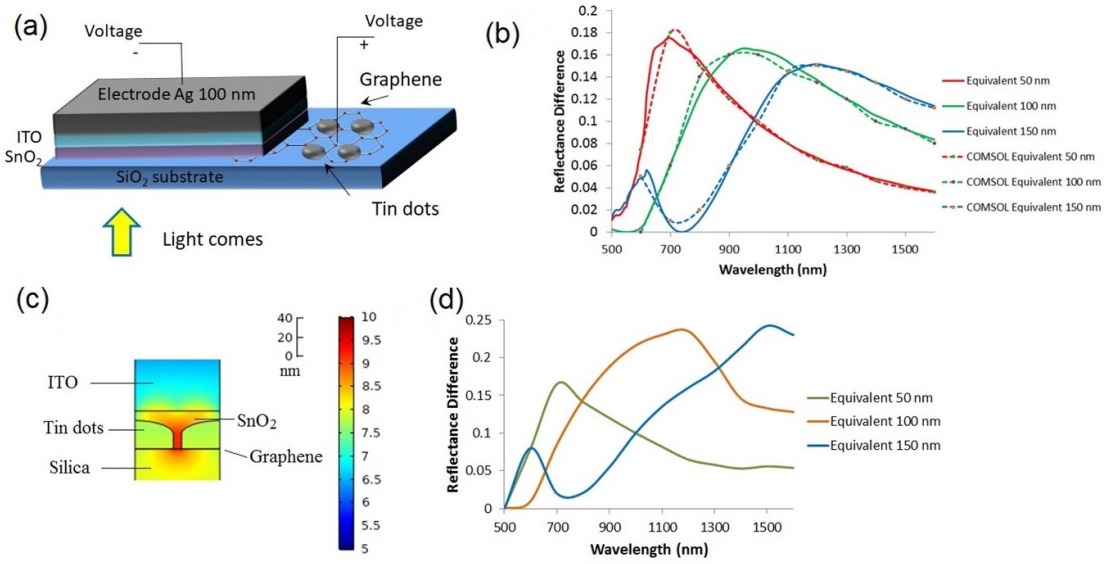

Figure 6. (a) The optimized resonator structure with tin nanodots and ITO layer added. (b) The reflectance difference with ITO layer but without tin dots. (c) The magnitude of the E-field plot. (d) The reflectance difference in the structure (a). The optical resonator keeps a good behavior with this optimization.

optical cavity length L, while electrically the dielectric layer thickness is contributed by the insulating SnO_2 layer only.

In this structure, the thickness of SnO_2 is fixed to be 10 nm, and the optical path depends on the thickness of ITO. To make the discussion continuously, we use the word 'equivalent 50/100/150 nm SnO_2', which means the optical path length is equivalent between the SnO_2/ITO and the SnO_2 structure. The actual thicknesses of ITO are 50/110/170 nm (without tin dots) and 10/70/130 nm (with tin dots) separately. Because of the lateral scattering effect of the Sn nanodots mentioned above, we have thinner ITO layer for the same effective optical path length when Sn nanodots are introduced. Figure 6(b) shows the reflectance difference by optical transition matrix model without tin dots. If we add tin dots, since the height of the Sn dots is 30 nm, the thicknesses of ITO are reduced. Figure 6(c) shows the magnitude of E-field plot with ITO layer added. The E-field is small inside the ITO layer, because ITO is conductive.

Comparing figures 6(b) and (d) with figures 5(b) and (d), the new structure keeps the characteristics of the optical cavity in both cases. Moreover, we add one more layer and create one more interface, so the reflectance difference will reduce a little because of interface reflectance loss. We have more losses in the infrared region, because the refractive index difference Δn between ITO and SnO_2 is larger in this region. Generally, the loss is just 0%−2% and will not have much influence in the optical cavity behavior.

We can calculate the voltage applied in this case,

$$\mathrm{U} = \frac{Q}{C} = \frac{\Delta p \mathrm{ed}}{\varepsilon_0 \varepsilon_\mathrm{r}}. \tag{11}$$

Set $\varepsilon_\mathrm{r} = 4.41, d = 10$ nm, $\Delta p = 1.125\ \mathrm{nm}^{-2}$(critical wavelength 600 nm), $U = 46.0$ V. If the critical wavelength is shifted to 1100 nm, the voltage will be greatly reduced to 4.5 V. In comparison, if the ITO layer is removed, the voltage value will be five times for the 50 nm SnO_2 optical cavity. We also did the simulations of the reflectance versus different Fermi levels for the equivalent 100 nm SnO_2 optimized structures. Figure 7 shows the results.

Comparing figure 7 with the refractive index values in figures 1(d) and (e), we can conclude that in the NIR region, we do not need an overly large driving voltage to achieve the maximum reflectance difference. After applying enough voltage to let graphene $k = 0$ at a given wavelength, the reflectance difference will saturate. Applying a larger voltage will only increase the tuning range but will not influence the reflectance difference for a specific wavelength. Figure 7(c) shows the plot of critical wavelength versus the driving voltage. In summary, the equivalent optical cavity length will determine where the maximum reflectance difference appears, and the driving voltage will affect the wavelength range of tuning. If we would like to achieve the maximum reflectance difference in the wavelength 1550 nm, we can use a 150 nm-equivalent optical cavity with the driving voltage 4.5 V as shown above.

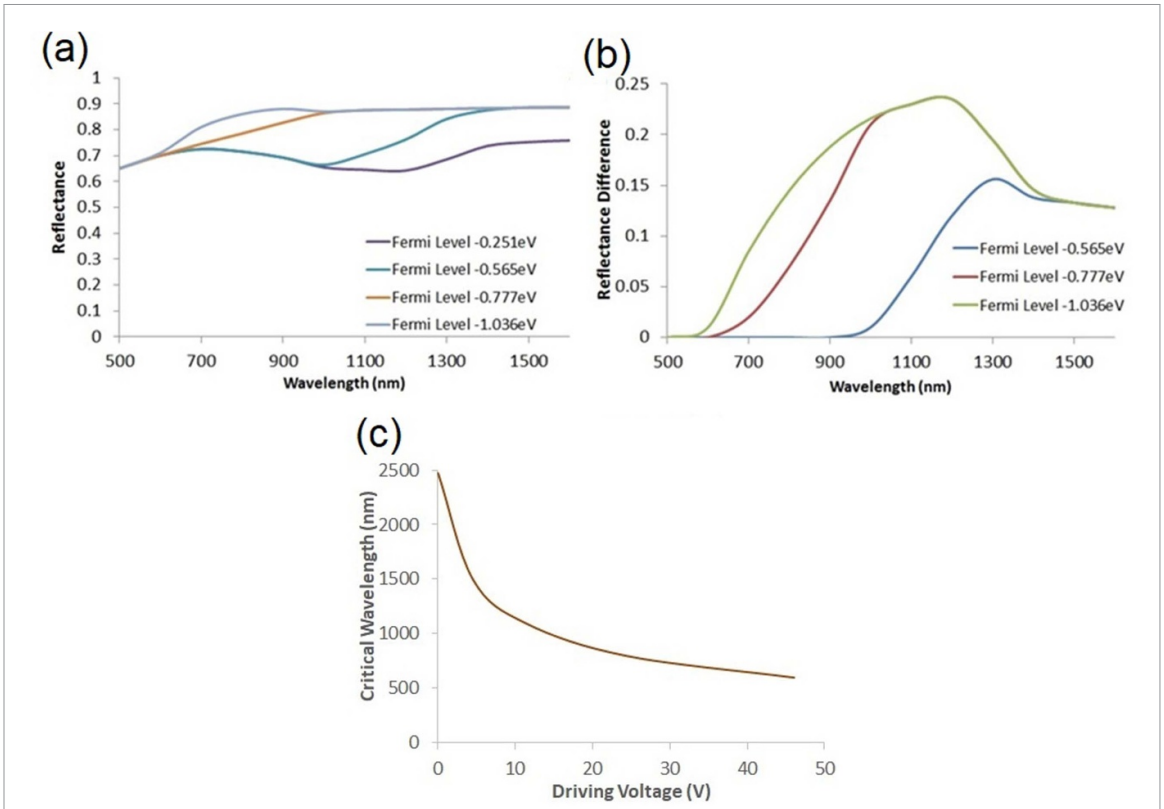

Figure 7. (a) Reflectance versus different Fermi levels for inherent graphene and three tuned graphenes. The structures are equivalent 100 nm SnO_2 optical cavities. (b) Reflectance difference between inherent graphene and three tuned graphenes. (c) Critical wavelength versus the driving voltage plot when the SnO_2 thickness is 10 nm. For a driving voltage on the graph, the reflectance difference will reach the maximum if the wavelength is larger than the critical wavelength.

The driving voltage can be further decreased by setting the SnO_2 thickness to 5 nm, and the value will reduce to one half. We preliminarily present these values here as a reference for future experiment work.

6. Conclusions

In this paper, we design a gate-tunable, free-space graphene electro-optical reflector working at NIR spectral regime based on cavity resonator structures. We calculate the graphene refractive index as a function of the Fermi level since there is a critical photon energy $\hbar\omega = 2E_F$ in this system. Then, we develop a theoretical model to describe the tuning difference. From this model, a backside reflector is needed and the reflectance should be as large as possible. We also select the dielectric materials next to graphene, which are SiO_2 and SnO_2, to optimize the optical performance while maintaining a good feasibility of device fabrication. We simulate this optical cavity by transfer matrix method, and the broadband, incident angle insensitive reflectance difference could reach 18%. We further increase this value to 28% with an extinction ratio 1.62 dB at a low insertion loss of 1 dB by incorporating tin nanodots based optical SAC structures. We also use conductive ITO layer as a part of the optical cavity and the electrode simultaneously to reduce the voltage applied. With an ITO layer, the optical cavity still shows a good property while the driving voltage can be reduced by a factor of 5. To our best knowledge, this is the first investigation on tunable free-space NIR reflectors based on 2D materials, rather than using liquid crystals or magnetic metasurfaces [41, 42]. Comparing to other graphene optical device simulated before, our structure is more feasible because it just needs a single graphene layer without graphene arrays or patterns [43–45]. Compared to other low-dimensional optical systems, such as TMDC, BP and metal-halide perovskites, graphene is air-stable, less poisonous [46, 47], and easier to fabricate at higher quality and larger area. Experimentally, the graphene layer can be transferred on the substrate by dry transfer or wet transfer method according to our pervious experimental work [8, 21, 25]. In the optimized design in figure 6(a), the deposition of Sn nanodots and SnO_2 on single layer graphene have also been demonstrated in our previous work [21, 24, 25], while the ITO and Ag layers can be further deposited on top of SnO_2 by evaporation or sputtering. The reflectance before and after gating can be measured by an optical spectrometer [21, 25]. The graphene Fermi level can be controlled by external gating, i.e. applying a voltage between the graphene layer and the Ag electrode (figure 6(a)). The graphene Fermi level and optical properties can be tuned by changing the gate voltage, as

discussed earlier in equations (1)–(7). Because our device is easier to fabricate and compatible with the free space optics, it has promising applications in tunable flexible photonic surfaces such as different kinds of VOAs or tunable reflectors for LiDAR systems [48].

Data availability statement

All data that support the findings of this study are included within the article (and any supplementary files).

Acknowledgments

We would like to thank Dr Weiling Dong and Dr Sidan Fu (Thayer School of Engineering, Dartmouth College) for their helpful discussions and suggestions in this project.

Author contributions

Jifeng Liu and Tao Fang initiated this project. Tao Fang did all the simulations. Xiaoxue Gao provided the spectrum for SnO_2 to calculate the refractive index. Xiaoxin Wang provided the original COMSOL source code for the Sn nanodots field enhancement simulations. The whole project was supervised by Jifeng Liu.

Competing financial interests

The authors declare no competing financial interests.

ORCID iDs

Tao Fang https://orcid.org/0000-0002-7008-5404
Jifeng Liu https://orcid.org/0000-0003-4379-2928

References

[1] Geim A K 2012 Graphene prehistory *Phys. Scr.* **T146** 014003
[2] Castro Neto A H, Guinea F, Peres N M R, Novoselov K S and Geim A K 2009 The electronic properties of graphene *Rev. Mod. Phys.* **81** 109–62
[3] Chaves F A and Jiménez D 2016 The role of the fermi level pinning in gate tunable graphene-semiconductor junctions *IEEE Trans. Electron Devices* **63** 4521–6
[4] Lherbier A *et al* 2012 Highly defective graphene: the thinnest insulating membrane *APS March Meeting*
[5] Ojeda-Aristizabal C, Bao W and Fuhrer M S 2013 Thin-film barristor: a gate-tunable vertical graphene-pentacene device *Phys. Rev.* B **88** 035435
[6] Jariwala D, Sangwan V K, Lauhon L J, Marks T J and Hersam M C 2014 Emerging device applications for semiconducting two-dimensional transition metal dichalcogenides *ACS Nano* **8** 1102–20
[7] Bhimanapati G R, Glavin N R and Robinson J A 2016 2D boron nitride: synthesis and applications *Semicond. Semimet.* **95** 101–47
[8] Fang T, Liu T, Jiang Z, Yang R, Servati P and Xia G 2019 Fabrication and the interlayer coupling effect of twisted stacked black phosphorus for optical applications *ACS Appl. Nano Mater.* **2** 3138–45
[9] Xu H, Xie L, Zhang H and Zhang J 2011 Effect of graphene fermi level on the Raman scattering intensity of molecules on graphene *ACS Nano* **5** 5338–44
[10] Nourbakhsh A, Cantoro M, Klekachev A, Clemente F, Sorée B, Van Der Veen M H, Vosch T, Stesmans A, Sels B and De Gendt S 2010 Tuning the fermi level of SiO2-supported single-layer graphene by thermal annealing *J. Phys. Chem.* C **114** 6894–900
[11] Stauber T, Peres N M R and Geim A K 2008 Optical conductivity of graphene in the visible region of the spectrum *Phys. Rev.* B **78** 085432
[12] Wang F, Zhang Y, Tian C, Girit C, Zettl A, Crommie M and Shen Y R 2008 Gate-variable optical transitions in graphene *Science* **320** 206
[13] Liu M, Yin X, Ulin-Avila E, Geng B, Zentgraf T, Ju L, Wang F and Zhang X 2011 A graphene-based broadband optical modulator *Nature* **474** 64
[14] Khandelwal H, Debije M G, White T J and Schenning A P H J 2016 Electrically tunable infrared reflector with adjustable bandwidth broadening up to 1100 nm *J. Mater. Chem.* A **4** 6064
[15] Deng T, Huang R, Tang M-C and Tan P K 2014 Tunable reflector with active magnetic metamaterials *Opt. Express* **22** 6287–95
[16] Dong W, Qiu Y, Yang J, Simpson R E and Cao T 2016 Wideband absorbers in the visible with ultrathin plasmonic-phase change material nanogratings *J. Phys. Chem.* C **120** 12713–22
[17] Wang X, Yu S, Zuo H, Sun X, Hu J, Gu T and Liu J 2021 Design of hybrid plasmonic multi-quantum-well electro-reflective modulators towards < 100 fJ/bit photonic links *IEEE J. Sel. Top Quantum Electron.* **27** 3400108
[18] Wang X, Yu S, Qin J, Cuervo-Covian A, Zuo H, Sun X, Hu J, Gu T and Liu J 2020 Low-voltage coupled multiple quantum well electroreflective modulators towards ultralow power inter-chip optical interconnects *J. Lightwave Technol.* **38** 3414–21
[19] Siegel D A, Park C-H, Hwang C, Deslippe J, Fedorov A V, Louie S G and Lanzara A 2011 Many-body interactions in quasi-freestanding graphene *Proc. Natl Acad. Sci.* **108** 11365–9
[20] Young S M and Kane C L 2015 Dirac semimetals in two dimensions *Phys. Rev. Lett.* **115** 126803
[21] Fu S, Wang X, Wang H, Gao X, Broderick K, Kong J and Liu J 2021 An optical slot-antenna-coupled cavity (SAC) framework towards tunable free-space graphene photonic surfaces *Nano Res.* **14** 1364–73

[22] Hwang C, Siegel D A, Mo S-K, Regan W, Ismach A, Zhang Y, Zettl A and Lanzara A 2012 Fermi velocity engineering in graphene by substrate modification *Sci. Rep.* **2** 590
[23] Ni Z, Wang Y, Yu T, You Y and Shen Z 2008 Reduction of Fermi velocity in folded graphene observed by resonance Raman spectroscopy *Phys. Rev.* B **77** 235403
[24] Yu X, Fu S, Song Y, Wang H, Wang X, Kong J and Liu J 2020 Color contrast of single-layer graphene under white light illumination induced by broadband photon management *ACS Appl. Mater. Interfaces* **12** 3827–35
[25] Fu S, Wang H, Wang X, Song Y, Kong J and Liu J 2019 Self-assembled, ultrahigh refractive index pseudo-periodic Sn nanostructures for broad-band infrared photon management in single layer graphene *ACS Photonics* **6** 50–58
[26] Ni Z H, Wang H M, Kasim J, Fan H M, Yu T, Wu Y H, Feng Y P and Shen Z X 2007 Graphene thickness determination using reflection and contrast spectroscopy *Nano Lett.* **7** 2758–63
[27] Ye S, Huang H, Yuan C, Liu F, Zhai M, Shi X, Qi C and Wang G 2014 Thickness-dependent strain effect on the deformation of the graphene-encapsulated Au nanoparticles *J. Nanomater.* **2014** 989672
[28] Xu F, Das S, Gong Y, Liu Q, Chien H-C, Chiu H-Y, Wu J and Hui R 2015 Complex refractive index tunability of graphene at 1550 nm wavelength *Appl. Phys. Lett.* **106** 031109
[29] Wang X, Chen Y P and Nolte D D 2008 Strong anomalous optical dispersion of graphene: complex refractive index measured by Picometrology *Opt. Express* **16** 22105–12
[30] Xia Q, Chen Z, Xiao P, Wang M, Chen X, Zhang J-R, Chen H-Y and Zhu J-J 2019 Fermi level-tuned optics of graphene for attocoulomb-scale quantification of electron transfer at single gold nanoparticles *Nat. Commun.* **10** 3849
[31] Johnson P B and Christy R W 1972 Optical constants of the noble metals *Phys. Rev.* B **6** 4370–9
[32] Rakić A D 1995 Algorithm for the determination of intrinsic optical constants of metal films: application to aluminum *Appl. Opt.* **34** 4755–67
[33] Ordal M A, Bell R J, Alexander R W, Long L L and Querry M R 1987 Optical properties of Au, Ni, and Pb at submillimeter wavelengths *Appl. Opt.* **26** 744–52
[34] Werner W S M, Glantschnig K and Ambrosch-Draxl C 2009 Optical constants and inelastic electron-scattering data for 17 elemental metals *J. Phys. Chem.* **38** 1013–92
[35] Golovashkin A I and Motulevich G P 1964 Optical and electrical properties of tin *Sov. Phys. JETP* **19** 310–7
[36] Johnson P B and Christy R W 1974 Optical constants of transition metals: Ti, V, Cr, Mn, Fe, Co, Ni, and Pd *Phys. Rev.* B **9** 5056–70
[37] Hagemann H-J, Gudat W and Kunz C 1975 Optical constants from the far infrared to the x-ray region: Mg, Al, Cu, Ag, Au, Bi, C, and Al2O3 *J. Opt. Soc. Am.* **65** 742–4
[38] Mak K F, Sfeir M Y, Wu Y, Lui C H, Misewich J A and Heinz T F 2008 Measurement of the optical conductivity of graphene *Phys. Rev. Lett.* **101** 196405
[39] Guo C, Zhang J, Xu W, Liu K, Yuan X, Qin S and Zhu Z 2018 Graphene-based perfect absorption structures in the visible to terahertz band and their optoelectronics applications *Nanomaterials* **8** 1033
[40] König T A F, Ledin P A, Kerszulis J, Mahmoud M A, El-Sayed M A, Reynolds J R and Tsukruk V V 2014 Electrically tunable plasmonic behavior of nanocube-polymer nanomaterials induced by a redox-active electrochromic polymer *ACS Nano* **8** 6182–92
[41] Meyer R B, Lonberg F and Chang C-C 1995 Liquid crystal smart reflectors *Smart Structures and Materials 1995: Smart Materials* vol 2441 (San Diego: Proc. SPIE) (https://doi.org/10.1117/12.209799)
[42] Badloe T, Mun J and Rho J 2017 Metasurfaces-based absorption and reflection control: perfect absorbers and reflectors *J. Nanomater.* **2017** Article ID 2361042
[43] Cao M, Wang T, Zhang H and Zhang Y 2018 Tunable electromagnetically induced absorption based on graphene *Opt. Commun.* **413** 73–79
[44] Liu Y, Zhong R, Lian Z, Bu C and Liu S 2018 Dynamically tunable band stop filter enabled by the metalgraphene metamaterials *Sci. Rep.* **8** 2828
[45] Niu Y, Wang J, Hu Z and Zhang F 2018 Tunable plasmon-induced transparency with graphene-based T-shaped array metasurfaces *Opt. Commun.* **416** 77–83
[46] Chen W, Zhang F, Wang C, Jia M, Zhao X, Liu Z, Ge Y, Zhang Y and Zhang H 2021 Nonlinear photonics using low-dimensional metal-halide perovskites: recent advances and future challenges *Adv. Mater.* **33** 2004446
[47] Pei J, Yang J, Yildirim T, Zhang H and Lu Y 2019 Many-body complexes in 2D semiconductors *Adv. Mater.* **31** 1706945
[48] Chung S W, Abediasl H and Hashemi H 2018 A monolithically integrated large-scale optical phased array in silicon-on-insulator CMOS *IEEE J. Solid-State Circuits* **53** 275–96